Formation of Task Representations and Replay in Mouse Medial Prefrontal Cortex

Hamed Shabani (1), Hannah Muysers (2), Yuk-Hoi Yiu (1,3,4), Jonas-Frederic Sauer (2,5), Marlene Bartos (1,2,3), Christian Leibold* (1,3,4)

(1) Bernstein Center Freiburg, University of Freiburg
(2) Institute for Physiology 1, Medical Faculty, University of Freiburg
(3) BrainLinks-BrainTools, University of Freiburg
(4) Faculty of Biology, University of Freiburg
(5) Systemic Neurophysiology, Center for Integrative Physiology and Molecular Medicine, Medical Faculty, Saarland University

*Correspondence should be addressed to
Christian Leibold, Bernstein Center Freiburg and Faculty of Biology, University of Freiburg, Hansastr. 9A, 79104 Freiburg i. Br., Germany
christian.leibold@biologie.uni-freiburg.de

Abstract

The medial prefrontal cortex (mPFC) is thought to support cognitive flexibility by forming and maintaining generalized representations of abstract tasks. The formation of these representations as well as their relation to preexisting representations of contextual or spatial information is incompletely understood. In this study, we analyzed longitudinal 1-photon calcium recordings in mice performing an olfaction-guided spatial memory task over an eight-week period that included habituation, training, and sleep epochs. Our results reveal that, while a minority of neurons initially conveyed significant information about the behavior of the animal, the bulk of task-related activity only emerged after the animals reached proficient performance. Although goal arm information is robustly represented at both the single-cell and network levels both during learning and in task proficient mice, it undergoes significant remapping throughout the learning process. Additionally, we identified the establishment of recurring sequences during learning and their replay at reward locations, with no evidence of them existing during odor sampling phase, during sleep or before training. Conversely, during odor sampling, information about odor identity is robustly available in the rate coactivation patterns, even before animals reached task proficiency. These findings suggest that the mPFC predominantly establishes generalized task representations de novo during learning, relying only minimally on preexisting spatial representations and that sub-second neural sequences in the mPFC are more likely involved in evaluating behavioral outcomes rather than planning future actions.

Introduction

The medial prefrontal cortex (mPFC) is generally implicated in the representation of abstract task variables [Miller & Cohen, 2001; Brincat et al., 2018, Kaefer et al., 2020; Tang et al., 2023; El-

Gaby et al., 2024] as required e.g., in rule learning [Wallis et al., 2001; Goodwin et al., 2012; Reinert et al., 2020]. In depth understanding of neuronal activity patterns associated with abstract tasks and their establishment during learning strongly profits from experimental approaches available in the rodent system. However, in addition to anatomical differences between primates and rodents [Laubach et al., 2018; Preuss & Wise, 2022; Hanganu-Opatz et al., 2023], behavioral task designs for rodents are also often affected by spatial components, which introduce correlations between task phases and spatial locations [Sauer et al., 2022; Muysers et al., 2024; Muysers et al., 2025]. On the one hand, this interrelation between space and task complicates interpretation of the results, on the other hand, it, however, also provides an opportunity to study potential effects of spatial schemas to task learning, as hypothesized from human fMRI data [Zheng et al., 2021]. Unlike in the hippocampus, where CA1 place cells undergo global remapping in different contexts, PFC representations have been found to remain stable across environments, allowing for task generalization [Tang et al., 2023, Muysers et al., 2024]. This stability suggests that new experiences do not completely overwrite PFC representations but instead integrates new information into existing structures, making the PFC a hub for cognitive flexibility. However, the precise nature of this reorganization remains debated. One perspective suggests that task representations in the PFC emerge de novo during learning and are distinct from preexisting spatial representations [Symanski et al., 2022]. This view is supported by findings that task-selective sequences arise only after learning, indicating a learning-driven transformation of PFC activity. An alternative perspective, however, argues that PFC task representations build upon preexisting spatial schemas rather than forming them entirely anew [Zheng et al., 2021]. Accordingly, the fact that PFC representations remain stable across environments may suggest that learning-related changes reflect adaptations of existing networks rather than the formation of entirely new assemblies within a circuit [Tang et al., 2021; Nardin et al., 2021]. Whether PFC task representations are reorganized from prior spatial schemas or develop independently remains unresolved, highlighting a fundamental gap in our understanding of cortical learning mechanisms.

In this study, we set out to study the development of task representations on longitudinal 1-photon recordings and to test whether they are based on preexisting spatial scaffolds. We reasoned that, in naive adult animals, task representations should only develop over learning, whereas the concept of space should be readily available during or even before training. We further addressed the question, whether task representations emerge as sequential assemblies in the mPFC network, or whether they are reflected as rate coactivation patterns. The former hypothesis would imply that pair correlations or activity sequences in neural populations could be interpreted as replay/preplay , whereas the latter would imply that aggregated task information would be available in population patterns and potentially provide a substrate for working memory.

Making use of a partly previously published dataset containing longitudinal mPFC recordings [Muysers et al., 2024, Muysers et al., 2025] over up to 8 weeks, encompassing habituation, training and sleep periods, we were able to explore the development of the task code during learning. We found a small subset of goal arm selective cells that develop general task selectivity and maintain the location of the place field. However, most of the task-related activity was observed only when the animals were proficient in task performance. Moreover, we found goal arm-selective information to be more strongly represented than general task phase information, both on the single

cell and the population level. A small fraction of goal arm-selective cells showed stable firing fields throughout the recording period even before learning has started. Establishing sequence analysis on calcium transients obtained from 1-p imaging, we identified the emergence of generalized task-selective sequences after learning, whereas we could find no evidence for task-related preplay during sleep or habituation to the arena. Both findings suggest that the mPFC task code is largely established during learning, with only a small amount of stable spatial tuning that is maintained from before learning.

Results

Mice learned to perform an odor-guided navigation task (Fig. 1A), while calcium activity was imaged in the mPFC using a miniscope [Muysers et al., 2024]. Depending on odor identity, mice had to learn to choose either the left or the right arm and were rewarded upon the correct choice. From previous analyses [Muysers et al., 2024, Muysers et al., 2025], we expected the recorded population to display place-specific activity and asked how many of the cells were significantly spatially informative after animals became proficient in the task. We employed a complementary approach to [Muysers et al., 2025] by testing for significance of spatial information content [Skaggs et al., 1993] (rate maps computed separately for left and right arm) with shuffle controls (see Methods), and only included data from outward runs. We found that about half of the cells were significantly informative (SI) about the goal-arm-specific location on the track. The place maps of SI cells, separately extracted from odd and even trials in the maze confirmed the statistical approach (Example animal in Fig. 1B). Since in this task, space is highly correlated with the task phase, we set out to distinguish place coding from task coding first, by training a Bayesian decoder on the whole population of recorded cells to predict goal-arm-specific spatial position based on the recorded activity (Fig. 1C). We found that the decoding error obtained by cross decoding (decoding left goal trajectories from the decoder trained on right goal trajectories and vice versa) had a similar magnitude as the error obtained from training and decoding on subsets of trials with the same goal arm (Fig. 1D). Both errors were considerably and significantly lower than those obtained from shuffle controls ($p<0.02$ for both errors; permutation test, 50 shuffles). To further corroborate the evidence that mPFC place coding has a high contribution of task-selective activity, we differentiated between goal-arm-selective and generalized task selective cells, computed rate maps separately for left- and rightward trials of SI cells (Fig. 1E) and computed correlation coefficients. Those SI cells for which the correlation exceeded the 95%-tile of the shuffle distribution (Methods) were called generalized task phase selective cells (TCs), whereas SI cells for which the two maps were not significantly similar were called goal-arm selective cells (GCs). We found a ratio of about 48% of TCs among SI cells (Fig. 1F) over all animals, considering only the “learned” sessions in which the animals have reached a performance criterion described previously (Methods; Muysers et al. (2024)).

In previous analyses generalized task-selectivity on the population level was shown to increase over learning (Muysers et al., 2025), we therefore examined how goal arm- and task phase-selectivity of SI cells develops over learning (Fig. 2). We therefore subdivided sessions into early “learning” sessions and late “learned” sessions based on a behavioral performance criterion of 70 % correct trials (Methods; Supplement to Figure 1A-C). During learning sessions animals had a strong bias

towards left turns (Fig. 2A; Supplement 1 to Fig. 2A), which was also reflected in the over proportionate number of SI cells with fields in leftward trials (Fig. 2B; Supplement 1 Fig 2B,C). After learning, both the behavioral and the neural biases vanished (Fig. 2A,B). New SI cells were predominantly added for rightward trials (Fig. 2B), whereas about a third of the SI cells for leftward trials did not remain SI in the learned condition (Fig. 2B). We then distinguished learning-induced changes between goal arm and task phase encoding cells and found that in learning trials there was a strong bias towards goal arm encoding (Fig. 2C), whereas in the learned condition a substantial fraction of TCs (about 40%) was consistently found in all animals (Fig 2C). The increase in generalized task phase encoding on the level of SI cells matches the increase of task phase encoding previously observed on the population level in an extended population of animals (path-equivalent cells in [Muysers et al., 2025]). Despite the growth of the TC population, GCs remained to be the majority of cells, particularly those GCs with a field in the stem (Fig. 2C). GCs on the stem have been previously referred to as splitter cells in the hippocampus [Wood et al., 2000] and suggested to encode episodic information. This is in line with our interpretation of GCs as goal encoding cells. Also only about 40% of initial TCs remained TCs after learning (Fig. 2C,D). The relative reduction in GCs, the increase in TCs and the instability of a fraction of TCs over learning indicates that emerging TCs in the learned condition may have been generated from previous GCs. Indeed ~40% of the TCs in the learned condition arose from GCs, however, also a similar fraction were not SIs during the learning condition (Fig. 2C,E). For GCs that became TCs in the learned condition, the majority kept their place field (in an interval +/- 0.1 relative to the original field center; see example place cell population in Fig. 2F and summary statistics in Fig. 2G). Thus, task coding develops over learning by addition of existing SI cells with already formed place fields as well as the acquisition of TCs from previously non-spatially tuned cells. However, although most of the selectivity arises over learning, a small but significant fraction of cells show stable rate maps not only in comparison between learning and learned conditions (Fig. 2G) but also taking into account the habituation phase, where the animals were exploring the behavioral arena without a task (Supplement 2 to Figure 2). A significant fraction of stable rate maps (habituation vs. learned) could particularly be observed in TCs but not in GCs (Supplement 2 to Figure 2F). This finding is consistent with the hypothesis of a limited preexisting scaffold.

We next reasoned that the establishment of a task code on the single cell level during learning will likely be associated with changes in covariance structure on the network level. Since a subpopulation of TCs inherited their firing fields from previous place fields, we reasoned that these initial firing properties could reflect the activity of previously existing cell ensembles. In a first set of analyses we were testing whether the rate covariance structure during the outward phase is “reactivated” in the sampling and reward phases using the reactivation measure proposed in [Peyrache et al., 2009; Peyrache et al., 2010] (Fig. 3). Both during learning and learned phase reactivation during sampling was significantly larger than during the reward phase (Wilcoxon test, Learning: p=0.016, rank=1, n=8 sessions, Learned: p=1.2e-10, rank=0, n=34 sessions), arguing that already during sampling cell assemblies active during outward running start to co-fire. Moreover, comparing reactivation of left or rightward patterns during sampling and reward phases in correct trials between a true goal (patterns were taken from the trials with fitting goal arm) and a swap goal (patterns were taken from the trials with opposite goal arm), reveals significantly stronger reactivation in the sampling period for the “true goal”, both for learning and learned condition

(Wilcoxon test; Learning: p=0.040, rank=3, n=8 sessions; Learned: p=2.4e-7, rank=30, n=34 sessions). These findings provide strong evidence that the cell assemblies during sampling are goal arm specific, i.e., could underlie a sensory-driven recall initiated by odor sampling. For the reward phase, reactivation reached significant goal arm specific only in the learned condition (Wilcoxon test; Learning: p=0.11, rank=6, n=8 sessions; Learned: p=7.2e-6, rank=56, n=34 sessions). Reactivation was significantly larger during sampling vs. reward even in the swapped condition (Wilcoxon test, Learning: p=0.032, rank=3, n=8 sessions, Learned: p=1.2e-5, rank=42, n=34 sessions), and reactivation strengths were not significantly different between learning and learned condition (Ranksum test; sampling: p=0.53, z=-0.64, n1=8, n2=34 sessions, reward: p=0.64, z=0.48, n1=8, n2=34 sessions; not shown in Figure), suggesting that the co-firing structure reflects olfactory cue rather than task information [Taxidis et al., 2020; Sun et al., 2024].

In addition to rate covariance (co-firing) based assemblies, mnemonic processes have also been associated with temporal activity pattern, i.e., activity sequences, particularly in the hippocampus. We therefore next applied an unbiased sequence detection algorithm (Chenani et al., 2019) based on z-scored rank order correlations. In order to select only time points with many concurrently active cells, we set a relatively permissive threshold to the population calcium traces (Methods) and extracted time intervals of 500 ms centered around the peaks of the population trace (Fig. 4A). Burst rates were significantly larger during behavioral epochs (covering about 20 to 40 % of the data thereby capturing large amount cofiring structure; Supplement to Figure 1 D, E) than during sleep and during periods of habituation to the arena (Task vs. sleep: $p = 3.1 \times 10^{-130}$, U = 4,974,538, n=7390; task vs. arena: $p = 2.6 \times 10^{-5}$, U = 1,546,011, n=6732 ; Mann-Whitney U rank tests; Fig. 4B), already indicating limited opportunities for preplay (i.e. behaviorally correlated sequences occurring before the start of the outward phase). Moreover, burst rates during correct trials were significantly lower than during error trials (p = 0.0014, U = 3461962, n=6292 ; Mann-Whitney U rank test; Fig. 4B). Ensembles were then identified according to the order of their center of mass calcium activity during population bursts (Fig 4C and Supplement 1 to Fig. 4A). Hierarchical clustering of the z-scored correlations was done longitudinally over all behavioral sessions during the learning and learned conditions based on similarity scores computed for all pairs of bursts in these times frames (Methods). With this approach we were able to identify repetitive activity sequences over the whole course of the experiment (see Rastermap plots [Stringer et al., 2019] Fig 4D; Supplement 2 to Fig. 4). The method is particularly reliable in identifying sequences of little active cells, whereas it may also falsely detect some sequence clusters of highly active cells (active in more than 50% of bursts); see Supplement 1 to Fig. 4B. Visual inspection of the Rastermap plots and correlating time points of sequence activations with behavioral trajectories exhibited large differences of sequence activation between learning and learned condition, both in the spatial patterns (example animal in Fig. 4D) and the distribution of the sequences (Fig. 4D,E). Rastermap plots (Fig. 4D) also reveal little similarity of sequence expression between task and habituation or sleep condition. Sequence expression during the task was more variable between learning and learned condition than between correct and error trials (Fig. 4E,F) as revealed from shuffled cluster identities (P-values were obtained using a permutation test with 200 shuffles: learning vs. learned, correct: p <0.005; failed: p <0.005; correct vs. failed, learning: p = 0.8350; learned: p = 0.415). Thus, our data suggest that task learning is associated with the establishment of a new robust population representation of current behavioral states.

In order to find functional correlates of the recurring sequence activity, we again computed SI values of sequence clusters and found a significant increase in SI clusters over learning (Wilcoxon signed rank test, $p = 0.02$, $W=1$, $n = 8$; Fig. 5A; Supplement 1 to Fig. 5A,B), similar to the increase in SI cells reported in Fig. 2B. Separating goal arm selective sequences (GS) from generalized task phase selective sequences (TS) by applying the same approach as for GCs and TCs (see Methods), we found an increase of both GSs and TSs over learning with a particular bias to goal specificity in the arm (Fig. 5B), different from the stem bias of GCs reported in Fig. 2C. The majority of sequence activity, however, was neither related to TSs nor to GSs (Fig. 5C). The only exception was during the outward runs, where GSs and TSs together contributed to sequence activity by about as much as non-SI sequences. To understand the origin of goal and generalized task phase tuning of sequence clusters we then examined the place fields of the contributing cells and found that particularly place fields in TCs had a stronger contribution to sequence activity in outward runs (Fig. 5D). Moreover, to link place fields of SI cells to fields of SI sequence clusters, we computed distributions of distances between the peak of the cluster field and place fields of the contributing cells (pooled histogram shown in Fig 5E; Histograms for individual animals in Supplement 1 to Fig 5C) and tested for significance, by comparing the distribution of peak distances between all cluster and cell fields. For all 7 detected TSs the field centers of the TCs significantly determined task tuning of the sequence clusters, whereas for the 13 GSs only less than the half were determined by the place field centers of GCs (Fig. 5F). Thus, there is a stronger link between TCs and TSs as compared to the link between GCs and GSs ($p = 0.0047$; Fisher's exact test).

Taken together, our findings suggest that recurring sequences during outward runs are largely supported by TCs, however, the overall frequency of their occurrence, and potentially their functional relevance for task representation is rather limited. We therefore were wondering, whether sequence activity correlates with trajectory replay as demonstrated for the hippocampus [Lee & Wilson, 2002]. By applying the Bayesian decoder generated for trajectory decoding from single cells (Fig 1C) trained on activity during population bursts (Fig 5G and Supplement 2 to Fig 5 for examples), we found correlations of decoded position with time bin (within a 500 ms burst) strongly exceeding chance level only during outward and reward phase, for both GSs and TSs (Fig 5H), with only fractions of significant forward replays exceeding chance levels. We reckoned that strong correlations between decoded position and time during outward phases may simply reflect the behavioral sequence (running trajectory, as in the first example shown in Fig 5G). We therefore computed decoding errors during bursts in outward runs (Fig. 5I) as root mean square error (RMSE) between true and decoded trajectories. The median RMSE of about 0.2 matches the RMSE from trajectory decoding in Fig.1D, supporting the interpretation that significant correlations between decoded position and time during SI sequences in outward runs in Fig. 5H reflect the real time task representation. Significant correlations of GSs and TSs in the reward phase, however, cannot relate to the current position of the animal and therefore have to be considered as replay. During the odor sampling phase, no such significant replay was observed for GSs and TSs suggesting these bursts are not involved in odor sampling or even planning, but rather in the execution and evaluation of behavior. Non-SI sequence clusters showed small but significant bias to preplay in the sampling phase, indicative of Non-SI sequence clusters potentially containing a small contribution of spatial subsequences. However, in contrast to GSs and TSs that show significant proportions of forward

replay (and not backward replay) in both the outward and reward phases, Non-SI sequences during sampling did not reveal significant forward preplays exceeding chance expectations, despite the presence of recurring sequence motifs. Replay was not significantly observable during the reward phase in the learning condition (Supplement 1 to Fig. 5D), which suggests that replay requires a stable task representation, or at least extensive exposure to the task. During the outward phase, however, correlations between decoded position and time were significant for all clusters (Supplement 1 to Fig. 5D), even for the non-SI clusters, supporting the interpretation of a real time behavioral representation even in the learning condition. Together with our finding of strong changes in sequence expression after learning (Fig 4E) these findings suggest that a representation of task develops during learning, however, it is not reflecting sequence structure during learning and habituation.

To conclude, generalized task phase representation by TCs developed in parallel to a goal arm representation by GCs, where the latter is supported by an even larger number of SI neurons (predominantly in the stem of the M-maze, i.e. splitter cells [Wood et al., 2000]) and an even larger amount of GSs (predominantly in the arm of the M-maze) than TSs. Thus, goal and task phase representation seem to coexist in rodent mPFC.

Discussion

Longitudinal measurements of 1-p calcium activity in mice learning and performing an odor-guided navigation task allowed us to analyze the development of goal arm and generalized task phase selectivity on the single cell as well as on the population level. Recordings from animals that have not yet reached good task performance exhibited a preference of goal arm selective neurons as compared to generalized task phase selective neurons. However, also in task proficient animals, with many generalizing TCs, a sizable amount of cells showed goal arm selectivity. GCs, however, largely remapped during learning, whereas TCs developed at least partly from initial SI cells with overlapping place fields, which indicates that those could be potential building blocks of task topology schemas. This hypothesis is further corroborated by a small but significant proportion of cells that exhibit a firing field at the same location in the arm even during habituation phase, without performing a task potentially indicative of cross-condition generalization. Extending our analysis to the coordinated activity of neural sequences, we found that learning leads to the emergence of new structured activity patterns, indicative of refined network organization. A large number of recurring activity motifs were present, but TSs almost exclusively arose after learning. These changes were not significantly different between correct and failed trials and suggest a broad reconfiguration of sequence dynamics in the mPFC. These findings support the idea that task representations are generated de novo in the mPFC during learning.

Our analyses are based on a previously analyzed data set [Muysers et al., 2024; 2025] and, using a complementary analysis approach, specifically confirm the main findings in [Muysers et al., 2025] regarding the higher stability and later development of TCs as compared to GCs. Our analyses extend the findings to habituation (no-task) periods, showing that a small fraction of TCs already has a firing field at the same position during habituation. Covariance and sequence-based analyses have not been performed in previous publications of this data set and show that the development of

a task representation specifically aligns with the formation of fast sequences, as well as their replay during reward.

While memory related fast (sub-second) sequence activity/temporally correlated firing has been previously reported in the PFC using electrophysiological methods [Euston et al., 2007; Fujisawa et al., 2008; Peyrache et al., 2009; Kaefer et al., 2020], the present study, to our knowledge, identified for the first time fast recurring neural sequence activity from 1-p calcium data, based on correlation analysis, thereby allowing to study the formation of fast sequences over a period of weeks. Using the center of mass approach for the calcium traces allows to interpolate between time samples and thereby limits the temporal resolution to the inverse of the sampling frequency rather than being constrained by the kinetics of the calcium indicator, at least for moderate sampling rates below about 50 Hertz.

So far, sequences on fast time scales have mostly been reported for the hippocampus during theta oscillations [Foster & Wilson, 2007] as well as during quiet wakefulness [Diba & Buzsaki, 2007; Foster & Wilson, 2006] and sleep [Lee & Wilson, 2002]; but see [Euston et al., 2007; Kaefer et al., 2020]. The functional role of hippocampal sequences is still debated and mostly assumed to relate to memory consolidation [Girardeau et al., 2009; Fernandez-Ruiz et al., 2019] and planning [Kay et al. 2020; Jadhav et al., 2012]. In contrast to hippocampal sequences, we find a very much reduced incidence rate outside the behavioral task, particularly during odor sampling. Odor sampling is a state of active sensing [Martin et al., 2007; Kay, 2014], and olfactory processing in PFC is not only reflected by co-firing patterns (Fig. 3 and [Taxisdis et al., 2020; Sun et al., 2024]), but has also been reported to affect oscillatory activity [Martin and Ravel, 2014], particularly phase amplitude coupling of beta and gamma oscillations to the theta rhythm [Ramirez-Gordillo et al., 2022]. The absence of preplay during the sampling phase is, thus, likely reflecting that active sensing and planning are distinct behavioral states. The absence of replay, and the generally low levels of sequence activity, during sleep/rest states suggests that they do not directly echo enhanced hippocampal sequence activity during sleep, questioning their role in consolidation. During outward runs, sequences seem to reflect the current behavioral state of the animal in the task and in space, corroborating that mPFC encodes task phase not only on the single cell level but also on the population level [Muysers et al., 2025]. These outward sequences could, thus, simply arise from trials with high firing rates. More interestingly though, is our finding on replay of GSs and TSs in the reward area. In contrast to the hippocampus where sequences of place cell activity are expressed in reversed order at the end of the track but in forward order at the beginning of the track [Diba & Buzsaki, 2007; Foster & Wilson, 2006] we found exclusively forward replay (Fig. 5H). Together with our finding of increased burst activity during error trials, this suggests that sub-second mPFC sequences may be associated with the evaluation of behavior. In addition to GSs and TSs, we found that most of the recurring sequences are not related to behavior (not SI), even during outward runs. Ongoing mPFC activity hence may reflect latent variables beyond experimental control.

The distinctiveness of hippocampal and PFC sequences has been emphasized previously [Kaefer et al., 2020; Nardin et al. 2023]. It is broadly assumed that mPFC sequences positively correlate with behavioral performance [Kaefer et al., 2020; Tang et al. 2021] – consistent with our observed establishment of stable task sequences after learning – and that they are associated with trajectory

reactivations [Tang et al. 2021; Nardin et al., 2023], which is consistent with our finding of enhanced trajectory indices in the reward area (Fig. 5H). However, the suggestion that mPFC sequences may also support planning [Tang et al., 2021], could not be confirmed by our work as sequences in the odor sampling phase were absent (Fig. 5H). The difficulty of interpreting planning-associated activity may also partly result from the many activity bursts that are not task-related (Fig. 5C) and the relatively smaller amount of GCs and TCs being active in the odor sampling phase during population bursts (Fig. 5D). Moreover, planning related sequences may be masked by activity related to active sensing. Additionally, the 1-p calcium signal may simply not be able to detect planning-associated activity in case it only relies on weak activity modulations.

In cognitive neurosciences, the prefrontal cortex is often assumed to support flexible behavior by schemas, i.e., prototypic behavioral patterns that can be applied under variable conditions that share the same important contextual aspect. PFC neural activity in rodents has also been linked to schemas when task structure remained stable across spatial locations [El-Gaby et al., 2024]. The use of schema-like activity during learning of a novel task, however, is only little investigated. A small sample of cells has previously been identified to maintain task structure during rule switching [Reinert et al., 2021]. While the limited subset of GCs we found to translate their place fields into a generalized task field over learning could be interpreted as potential building blocks of schema of the spatial environment, task-related activity mostly developed independently from previous spatial representations. We thus hypothesize that in order to transfer a larger degree of schema-related representations to a new task, higher behavioral similarity between the tasks is required.

Methods

Experimental data was mostly published previously in Muysers et al. (2024) and Muysers et al (2025). Data derived from periods of sleep and habituation to the arena are previously unpublished. Detailed description of experimental methods can be found in the original publication. The next paragraph only provides a brief summary.

Experimental Methods and Data Preprocessing. Data was derived from 4 Thy1-GcaMP6f mice (Jackson Labs #025393; 2 female & 2 male). Animals were 11 weeks (75-78 days) old upon lens implantation and 16 weeks upon the beginning of the handling. The analyzed animals represented the subset of the previously published animals (Muysers et al., 2024, 2025) for which sufficiently many cells could be tracked throughout the experiment (including sleep and arena) to perform longitudinal sequence clustering.

Animals were first habituated to the experimenter and the experimental room for at least three days. The animals were then exposed to the behavioral arena (M-shaped maze) for three days (habituation to arena). The two different odors (vanilla; coconut) and the reward were introduced subsequently and the animals were exposed for a week to ‚forced‘ trials: The odor was presented at the center arm of the arena and only the correct door to the respective side-arm was opened, a reward was consequently given at the end. Thereafter, the “free choice” trials started, where the odor was presented at the center and both side-arms were accessible for free choice. Animals were trained for

two months. In this time, all four mice learned the task (≥70% correct across three consecutive days).

Behavioral epochs (sampling, center, side, reward, all for left and right respectively) of the task were extracted, based on xy-thresholds of arena locations obtained from camera tracking.

Integrated GRIN lenses of ø 1mm (Inscopix #1050-004637) were used to gain optical access to the prefrontal cortex via a ø ~1mm craniotomy above the mPFC (centering on 1.7 mm anterior and 0.6 mm lateral of bregma).

Neuronal activity was recorded when the animals were first exposed to the behavioral arena and throughout all training sessions. For analysis we focused on the recordings of three days freely moving in the arena, four days of learning (~50% correct trials) and four days after reaching the criterion ("learned"). Additionally, animals were recorded during sleep in their homecage before and after learning of the task.

The open source Python toolbox Caiman was used to identify neurons in the recorded 1-photon videos. Extracted components were manually checked (https://github.com/chenhungling/CaimanGUI) before further analysis.
Calcium traces, as extracted with Caiman, were first corrected for slow drifts using a running percentile filter (10th percentile, 30s window). The mean (baseline) and standard deviation (σ) were then calculated iteratively. In each iteration, signal above 3σ was excluded and baseline and σ was calculated again until the relative change in σ was smaller than 0.1%. The traces were baseline-subtracted and normalized by the respective σ.

Significant transients were detected by keeping signal >3σ and a minimum duration of 0.2 s. The rest of the signal was set to 0. CellReg was used to track cells across sessions (Sheintuch et al., 2017).

Reactivation analysis. We followed Peyrache et al., (2010) and computed reactivation strength R_l of a population pattern b_l evoked by z-scored activity population vectors z (during sampling or reward) according to $R_l = (b_l^T z)^2$, with b_l denoting the l-th significant eigenvector of the n x n covariance matrix of the z-scored activity vectors during the outward (task) phase (with n denoting the number of simultaneously recorded neurons). Time binning was extended to 250ms and only those session were used in which the total duration of outward phase for each trial type (left/right) was exceeding 12.5s. Significance of eigenvectors was assessed via the Marchenko-Pastur bound $(1+(n/T)^{1/2})^2$, with T denoting the number time samples. Total reactivation R was then calculated as the weighted sum of all time averaged R_l, weighted with the corresponding eigenvalue of pattern b_l.

Burst detection. The population activity for each recording session was calculated by summing the neuronal activity across neurons at each time point. Subsequently, for each animal, the population activity from all sessions was concatenated to estimate the overall activity.
Burst events were identified when population activity exceeded a threshold of 0.5 standard deviations (σ). Neural activity from active cells within a 500 ms window, centered on each burst, was extracted and cells were sorted based on the center of mass time point of the calcium trace. For each population burst, the sorted indices of these cells were compiled into individual sequence vectors. Only sequences comprising at least five cells were included in subsequent analyses. Using the center of mass inherently normalizes for heterogeneous firing rates among neurons, a factor that can lead to spurious sequence order in electrophysiological recording, because high firing neurons would always fire earlier.

Clustering sequences. To quantify the similarity between sequence pairs, Spearman's rank correlation coefficients were calculated based on the ordinal ranks of neuron activations in each pair of bursts. Only the L neurons active in both sequences of a pair were taken into account. By construction Spearman's correlations are symmetric. In order to check for significance of sequence similarity, we followed the approach detailed in (Chenani et al., 2019): Correlations values were z-scored according to the distribution of correlation coefficients derived from random sequences of same length L (i.e., all permutations of the sequence [0,1,2,…,L]). Only pairs with significant z score were considered further. The resulting binary matrix (1: significant, 0: non-significant) was then used for agglomerative hierarchical clustering with Ward's linkage method, producing discrete sequence clusters.

Iterative merging of cluster templates. After initial clustering of sequences and construction of a template for each cluster by averaging its member bursts, we quantified cluster similarity using the procedure described above for individual sequences. At each iteration we identified the cluster pairs with significant similarity and merged their underlying members if they were too similar, i.e., the z-score of a template pair exceeded a value of 2.5. Following each merge, cluster templates and similarity matrix were recomputed, and the procedure was repeated until no pair of clusters satisfied the merging criterion. The workflow for cluster identification is summarized in Figure 6.

Occupancy. Occupancy was calculated by first generating a histogram of the animal's position. The counts in each bin of the histogram were multiplied by the time spent in the corresponding bin, converting position counts into occupancy values per bin. To smooth the occupancy data, a Gaussian filter with sigma = 5 cm was applied.

Rate map. The smoothed transient histogram was divided by the occupancy to obtain the firing rates for each position bin.

Spatial information. Spatial information was calculated using the rate maps of neurons to identify place cells:

$I = \sum_x P(x) \cdot r(x) \cdot \log_2((r(x) + \varepsilon) / (r_0 + \varepsilon))$

Where r(x) is the firing rate in a spatial bin x, P(x) is the probability of the animal being in bin x, $r_0$is the overall mean firing rate, and ϵ is a small constant (1e-10) to prevent division by zero.

To identify place cells with significant spatial information, we performed circular shuffling of transient times within each trial period and calculated the spatial information for the shuffled rate maps. This process was repeated 500 times, generating 500 shuffled datasets. The spatial information of the original data was then compared to the shuffled distributions. Neurons with spatial information significantly greater than the shuffled data were classified as spatially informative (SI) cells.

Bayesian decoder. A Bayesian decoder was employed to calculate the posterior probabilities of all position bins. This method assumes that transient counts follow a Poisson distribution and combines transient counts and rates to compute the likelihood of the animal being at each position bin, given by:

$\log L(y) = \sum_{i=1}^{N} [\, k_i \log(r_i(y) \cdot \Delta t) - r_i(y) \cdot \Delta t - \log(k_i!) \,]$

Where L(y) is the likelihood of the animal being at position y, N is the total number of neurons, k_i is the count of transients of neuron i, $r_i(y)$ is the mean transient rate of neuron i at position y, and Δt is the decoding time bin.

The posterior probability P(y) is obtained by normalizing the likelihoods across all position bins:

$P(y) = L(y) / \sum_{y'} L(y')$

The estimated position of the animal is determined as the position ŷ that maximizes the posterior probability $\hat{y} = \mathrm{argmax}_y P(y)$.

Position estimation. To estimate the animal's position, peaks of transient calcium traces were detected for each neuron. Peak detection was performed using the find_peaks function from Python's SciPy library, with the parameters set to height=0, width= 50ms, and distance = 100 ms. The height=0 parameter ensured that all peaks above zero were considered, width specified the minimum width of peaks to be detected, and distance set the minimum required distance between consecutive peaks to avoid detecting closely spaced events as separate peaks.

A Bayesian decoder was trained using the detected peaks that were not part of bursts or their neighboring points. The decoder was then tested on the time points where bursts occurred to estimate the animal's position.

Estimate position using burst data. To estimate the animal's position using burst signals of sequences, a Bayesian decoder was trained using rate maps from outward runs as the training data. Time points when sequences were detected were excluded from the training data to ensure that the decoder's training was not influenced by these events. The decoder was then tested exclusively on the 500 ms burst signals centered around the detected sequences. Event times of bursts during the sampling, outward, and reward periods were used as test data. The animal's position during these times was estimated by taking the maximum likelihood of the posterior probability distribution provided by the Bayesian decoder.

Subsampling. To account for the unequal number of trials between the learning and learned conditions, the number of sequences in the learned condition was equalized by subsampling. The learned data were subsampled to match the number of sequences in the learning condition. This process was repeated 50 times to ensure robustness. Clustering was then performed independently on each of the 50 subsampled datasets.

Kullback-Leibler (KL) Divergence. To quantify the differences in cluster distributions between the learning and learned conditions, the Kullback-Leibler (KL) divergence was applied. The KL divergence is defined as $DKL(P \parallel Q) = \Sigma_i P(i) \log(P(i) / Q(i))$, where P(i) and Q(i) represent the probabilities of sequence cluster i during the learning and learned conditions, respectively.

The KL divergence was calculated for each of the 50 subsampled datasets, resulting in a distribution of KL values derived from the original data. To assess significance, a null distribution was generated by randomly assigning sequences to the learning and learned conditions and computing the KL divergence for 50 such shuffled datasets. The KL divergence from the original data was considered significant if it exceeded the 95th percentile of the null distribution.

Assigning sleep and arena sequences to clusters. Assignment of sleep, arena, and task sequences to clusters was performed by calculating the rank order correlation between each sequence and all cluster templates. Each sequence was then assigned to the cluster with the highest similarity score based on the computed correlations.

Cluster-to-Cell Distance. The distances between cells and clusters were calculated by measuring the differences between the peak positions of the cells' rate maps and the sequence cluster templates. Distances were histogrammed for two conditions: either cell and sequence cluster are of same type (task arm, task stem, place arm, place stem) or including all cells. The two resulting distributions of distances were compared using a two-sided Mann–Whitney U test.

Task Cells and Goal arm Cells. To classify SI cells as goal arm selective cells or generalized task phase selective cells based on their firing patterns, rate maps during both left and right runs were analyzed. Cells were first sorted according to their rate maps from left runs. The analysis was then repeated, sorting cells according to their rate maps from the right run. For both sorting conditions, correlation coefficients were computed between the sorted rate maps of left and right runs for each region. To assess significance, a null distribution was generated by computing correlations between the rate maps of one condition and cell-index shuffled rate maps of the other condition. Cells with correlation coefficients exceeding the 95th percentile of this null distribution were classified as significant TCs, indicating similar activity during left and right runs. Conversely, cells with lower correlations were classified as GCs.

The rate maps were divided into two regions: the stem (linearized position 0–0.5) and the arms (0.5–1). Hence, the analysis identified four cell types: GCs in the arms (GC-arm), GCs in the stem (GC-stem), task cells in the arms (TC-arm), and task cells in the stem (TC-stem).

Task Sequences and Goal arm Sequences. Criteria for defining GCs and TCs were also applied to categorize clusters based on their firing patterns and spatial activity into goal arm selective sequence clusters (GS) and generalized task phase sequence clusters (TS): Firing rate maps were computed for each cluster. Only clusters were further considered for which the at least one of the firing rate maps (Right/Left) had a significant SI. Rate maps were then correlated between left and right trials. If the correlation coefficient exceeded the 95 percentile of a cell index shuffle the clusters was considered a TS, otherwise a GS. The analysis was restricted to clusters containing at least five sequences.

Stability of place fields. To assess the stability of firing fields after learning, we compared the rate maps of SI cells between learning and learned condition. For each cell, the rate map of one condition was circularly shifted, and the correlation between the shifted and original maps was computed. If the maximum correlation occurred within a shift range of ±0.1, the cell was considered stable.

Data and Code availability

Analysis code is available from the GitHub-Repository https://github.com/HamedShabani/PFC_sequence_analysis. The datasets that went into the analyses are available under https://doi.org/10.12751/g-node.b8k1yn. Part of the data is overlapping with the repository of a previous publication (https://doi.org/10.5281/zenodo.10528243).

Acknowledgments

This work was funded by the German Research Association (DFG) under grant numbers LE2250/20-1 (C.L., FOR5159), BA 1582/16-1 (M.B. FOR5159), BA 1582/24-1 (M.B.), and SA 3609/2-1 (J-F.S.FOR 5159).

References

Brincat SL, Siegel M, von Nicolai C, Miller EK. (2018) Gradual progression from sensory to task-related processing in cerebral cortex. Proc. Natl Acad. Sci. USA. 115:E7202–E7211.

Chenani A, Sabariego M, Schlesiger MI, Leutgeb JK, Leutgeb S, Leibold C. (2019) Hippocampal CA1 replay becomes less prominent but more rigid without inputs from medial entorhinal cortex. Nat Commun. 10:1341.

Diba K, Buzsáki G (2007). Forward and reverse hippocampal place-cell sequences during ripples. Nat Neurosci 10:1241-2.

El-Gaby M, Harris AL, Whittington JCR, Dorrell W, Bhomick A, Walton ME, Akam T, Behrens TEJ. (2024) A cellular basis for mapping behavioural structure. Nature 636:671-680.

Euston DR, Tatsuno M, McNaughton BL. (2007) Fast-forward playback of recent memory sequences in prefrontal cortex during sleep. Science 318:1147-50.

Foster DJ, Wilson MA. (2006) Reverse replay of behavioural sequences in hippocampal place cells during the awake state. Nature. 440:680-3.

Foster DJ, Wilson MA. (2007) Hippocampal theta sequences. Hippocampus. 17:1093-9.

Fernández-Ruiz A, Oliva A, Fermino de Oliveira E, Rocha-Almeida F, Tingley D, Buzsáki G. (2019) Long-duration hippocampal sharp wave ripples improve memory. Science 364:1082-1086.

Fujisawa S, Amarasingham A, Harrison MT, Buzsáki G. (2008) Behavior-dependent short-term assembly dynamics in the medial prefrontal cortex. Nat Neurosci 11:823-33.

Girardeau G, Benchenane K, Wiener SI, Buzsaki G, and Zugaro MB (2009). Selective suppression of hippocampal ripples impairs spatial memory. Nat Neurosci 12:1222–1223.

Goodwin SJ, Blackman RK, Sakellaridi S, Chafee MV. (2012) Executive control over cognition: stronger and earlier rule-based modulation of spatial category signals in prefrontal cortex relative to parietal cortex. J. Neurosci 32:3499–3515.

Hanganu-Opatz IL, Klausberger T, Sigurdsson T, Nieder A, Jacob SN, Bartos M, Sauer JF, Durstewitz D, Leibold C, Diester I. (2023) Resolving the prefrontal mechanisms of adaptive cognitive behaviors: A cross-species perspective. Neuron 111:1020-1036.

Jadhav SP, Kemere C, German PW, Frank LM. (2012) Awake hippocampal sharp-wave ripples support spatial memory. Science 336:1454-8.

Kaefer K, Nardin M, Blahna K, Csicsvari J. (2020) Replay of Behavioral Sequences in the Medial Prefrontal Cortex during Rule Switching. Neuron 106:154–165.

Kay LM. (2014) Circuit oscillations in odor perception and memory. Prog Brain Res. 208:223-51

Kay K, Chung JE, Sosa M, Schor JS, Karlsson MP, Larkin MC, Liu DF, Frank LM. (2020) Constant Sub-second Cycling between Representations of Possible Futures in the Hippocampus. Cell 180:552-567.e25.

Laubach M, Amarante LM, Swanson K, White SR. (2018) What, If Anything, Is Rodent Prefrontal Cortex? Eneuro 5:ENEURO.0315-18.2018.

Lee AK, Wilson MA. (2002) Memory of sequential experience in the hippocampus during slow wave sleep. Neuron 36:1183-94.

Martin C, Beshel J, Kay LM. (2007) An olfacto-hippocampal network is dynamically involved in odor-discrimination learning. J Neurophysiol. 98:2196-205.

Martin C, Ravel N. (2014) Beta and gamma oscillatory activities associated with olfactory memory tasks: different rhythms for different functional networks? Front Behav Neurosci. 8:218.

Miller EK, Cohen JD (2001). An integrative theory of prefrontal cortex function. Ann Rev Neurosci 24: 167-202.

Muysers H, Chen HL, Hahn J, Folschweiller S, Sigurdsson T, Sauer JF, Bartos M. (2024) A persistent prefrontal reference frame across time and task rules. Nat Commun. 15:2115.

Muysers H, Bartos M, Sauer JF (2025) Conjoint generalized and trajectory-specific coding of task structure by prefrontal neurons. Cell Rep (accepted for publication).

Nardin M, Kaefer K, Csicsvari J (2021). The generalized spatial representation in the prefrontal cortex is inherited from the hippocampus. BioRxiv 2021.09.30.462269.

Nardin M, Kaefer K, Stella F, Csicsvari J. (2023) Theta oscillations as a substrate for medial prefrontal-hippocampal assembly interactions. Cell Rep 42:113015.

Peyrache A, Khamassi M, Benchenane K, Wiener SI, Battaglia FP. (2009) Replay of rule-learning related neural patterns in the prefrontal cortex during sleep. Nat Neurosci. 12:919-926.

Peyrache A, Benchenane K, Khamassi M, Wiener SI, Battaglia FP. (2010) Principal component analysis of ensemble recordings reveals cell assemblies at high temporal resolution. J Comput Neurosci. 29:309-325.

Preuss TM, Wise SP. (2022) Evolution of prefrontal cortex. Neuropsychopharmacology. 47:3-19.

Ramirez-Gordillo D, Bayer KU, Restrepo D (2022). Hippocampal-prefrontal theta coupling develops as mice become proficient in associative odorant discrimination learning. Eneuro 9:ENEURO.0259-22.2022.

Reinert S, Hübener M, Bonhoeffer T, Goltstein PM. (2021) Mouse prefrontal cortex represents learned rules for categorization. Nature. 593:411-417.

Sauer JF, Folschweiller S, Bartos M. (2022) Topographically organized representation of space and context in the medial prefrontal cortex. Proc Natl Acad Sci U S A 119:e2117300119.

Sheintuch L, Rubin A, Brande-Eilat N, Geva N, Sadeh N, Pinchasof O, Ziv Y (2017). Tracking the Same Neurons across Multiple Days in Ca^{2+} Imaging Data. Cell Rep. 21:1102-1115.

Skaggs WE, McNaughton BL, Gothard KM, Markus EJ (1993) An information-theoretic approach to deciphering the hippocampal code. In: Advances in neural information processing 5 (SJ Hanson, JD Cowan, CL Giles, eds), pp 1030–1037. San Mateo, CA: Morgan Kaufmann Pub.

Stringer C, Pachitariu M, Steinmetz N, Reddy CB, Carandini M, Harris KD (2019) Spontaneous behaviors drive multidimensional, brainwide activity. Science, 364: eaav7893.

Sun Y, Takehara-Nishiuchi K. (2024) The medial prefrontal cortex leaves the hippocampus when it prepares for the future. Sci Prog. 107:368504241261833.

Symanski CA, Bladon JH, Kullberg ET, Miller P, & Jadhav SP (2022). Rhythmic coordination and ensemble dynamics in the hippocampal-prefrontal network during odor-place associative memory and decision making. Elife, 11:e79545.

Tang W, Shin JD, Jadhav SP. (2021) Multiple time-scales of decision-making in the hippocampus and prefrontal cortex. Elife 10:e66227.

Tang W, Shin JD, Jadhav SP. (2023) Geometric transformation of cognitive maps for generalization across hippocampal-prefrontal circuits. Cell Rep 42:112246.

Taxidis J, Pnevmatikakis EA, Dorian CC, Mylavarapu AL, Arora JS, Samadian KD, Hoffberg EA, Golshani P. (2020) Differential Emergence and Stability of Sensory and Temporal Representations in Context-Specific Hippocampal Sequences. Neuron 108:984-998.e9. d

Wallis JD, Anderson KC, Miller EK. (2001) Single neurons in prefrontal cortex encode abstract rules. Nature 411:953–956.

Wood ER, Dudchenko PA, Robitsek RJ, Eichenbaum H. (2000) Hippocampal neurons encode information about different types of memory episodes occurring in the same location. Neuron 27: 623-633.

Zheng L, Gao Z, McAvan AS, Isham EA, Ekstrom AD. (2021) Partially overlapping spatial environments trigger reinstatement in hippocampus and schema representations in prefrontal cortex. Nat Commun. 12:6231.

Figures

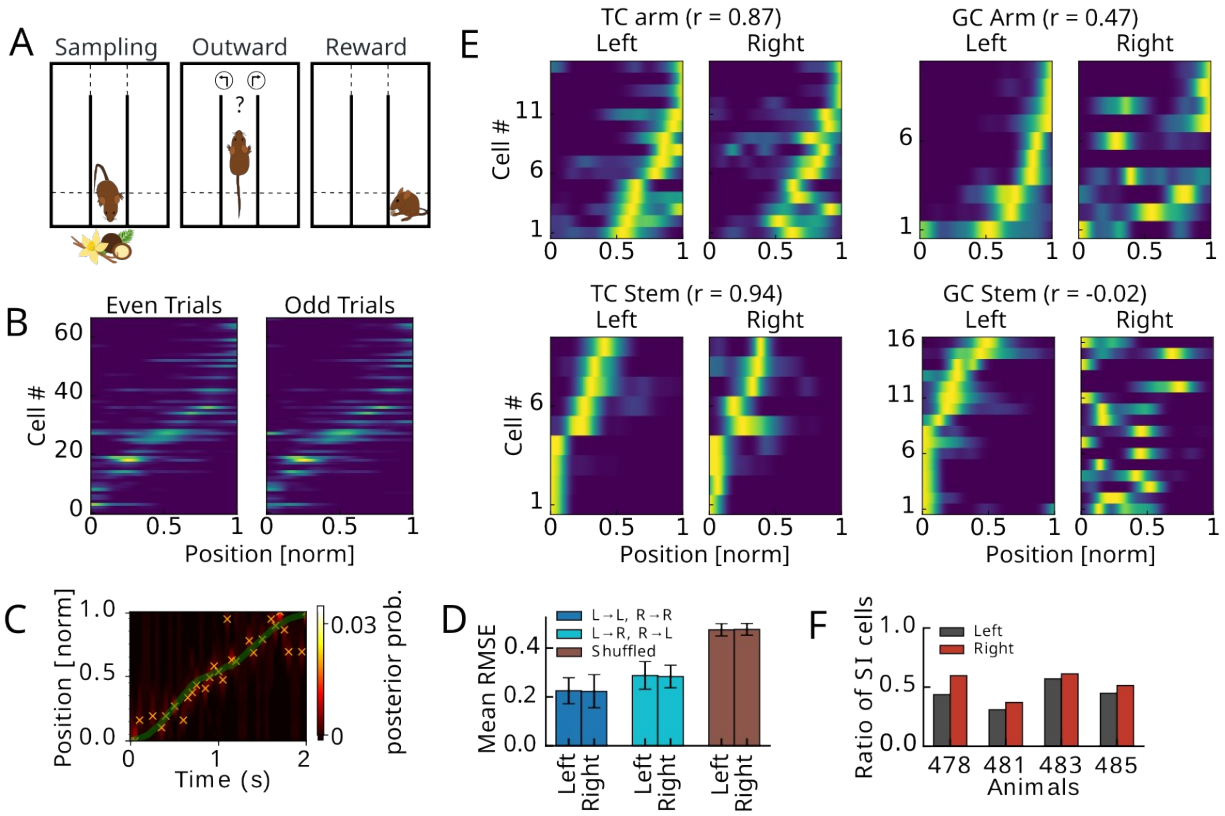

Figure 1. Spatially informative mPFC principal cells from proficient mice performing an odor guided navigation task. (A) Mice were performing an odor guided navigation task. We separated analysis into three behavioral phases. During Sampling animals were exposed to an odor. During Outward the animals were moving on the stem and one of the arms (above dashed line). During Reward the animals were in the reward area (below dashed line). (B) Activity maps (computed separately for left and right arm) obtained from 1-photon calcium imaging were tested on significant spatial information (SI) content. Maps of cells with significant SI (example session) are matching between even and odd trials. (C) Example trial in which maximum posterior decoding (crosses) is aligned with true position (green). (D) Root mean square decoding errors (RMSE) for all animals and all session separated for left and right arm trajectories. Cross decoding RMSE (light blue) is still significantly lower than RMSE from shuffling ($p<0.02$; none in 50 cell index shuffles), indicating a large contribution of left-right invariant, i.e. task phase selective activity. (E) Recordings from an example animal 485 separated into generalized task phase selective cells (left) and goal arm selective cells (right) with left and right activity maps significantly correlated or not. (F) About half of the cells are significantly spatially informative in all animals.

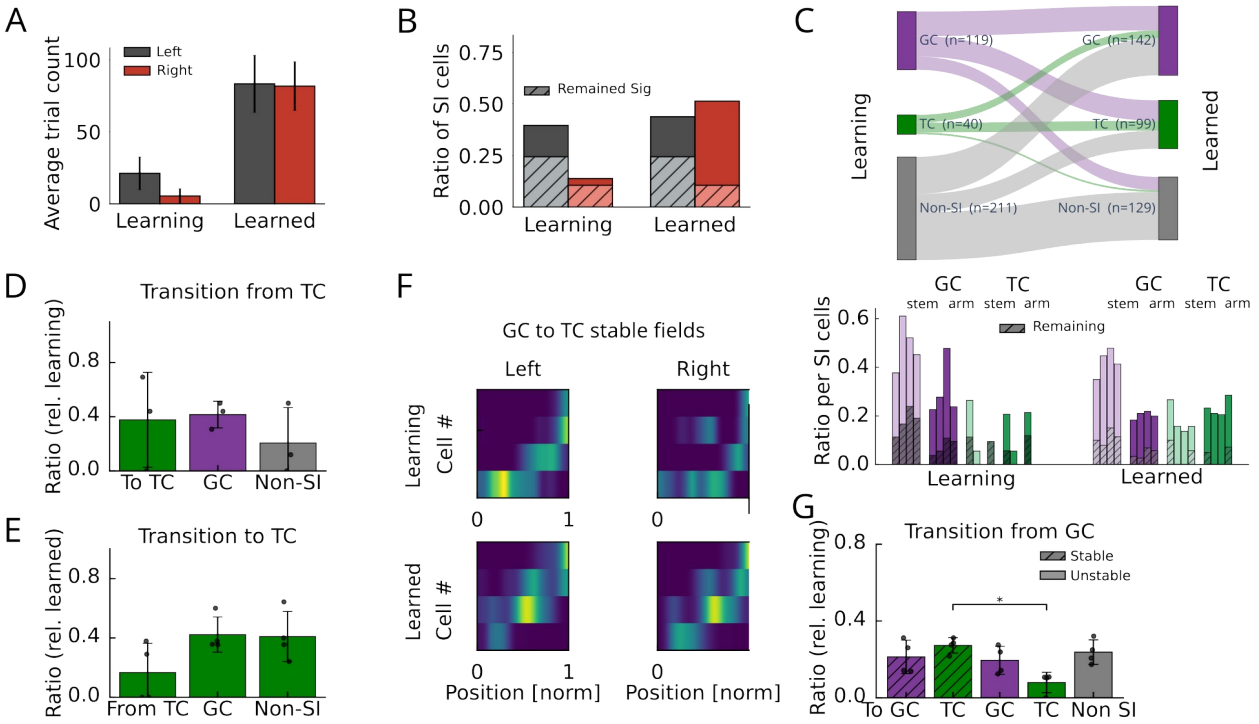

Figure 2. Development of task tuning during learning, (A) Trial counts (mean and standard deviation) over all animals in the learning and learned condition. Recordings in both conditions were limited to 15 minutes, explaining the lower number of trials in the learning group, where animals are still familiarized with the task structure. (B) Fraction of SI cell averaged across animals in the learning and learned condition. Hatched areas indicate proportions significant in both conditions (overlapping cells). (C) Top: Transition between different cell types between learning and learned sessions. Bottom: Amount of GCs and TCs normalized by the number of SI cells for all 4 animals (individual bars) during learning and learned condition. Hatched areas indicate proportions of cells that remain in the same category after learning. (D) Fractions of task cells (during learning) that transitioned to TC, GC and non-SI cells after learning. (E) Fraction of task cells (for the learned condition) that arose from TC, GC and non-SI cells during learning. (F) Example of GCs during learning (in one animal) that became TCs after learning. (G) Fractions of GCs (during learning) that transitioned to TC, GC and non-SI cells with stable (hatched) and non-stable (plain) place field location. A Wilcoxon signed rank test showed significantly larger ($p = 0.028$, $U=0$, $N=4$ animals) stable TCs than non-stable TCs.

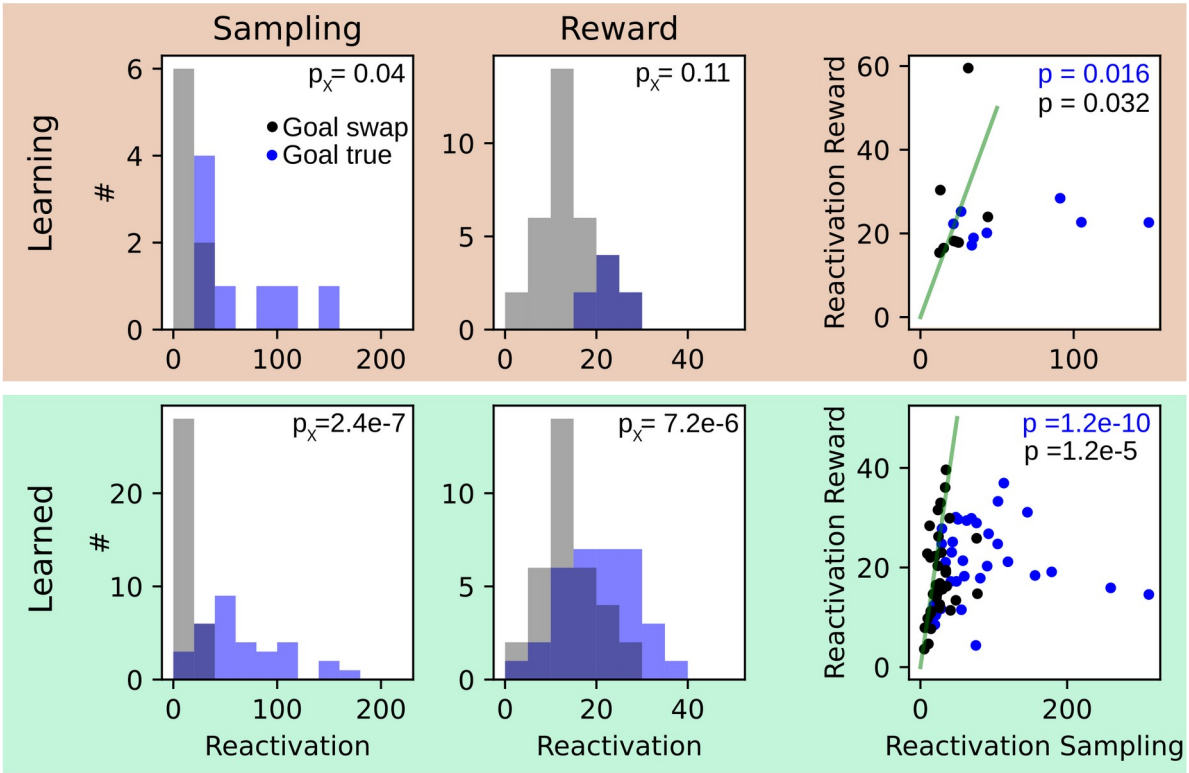

Figure 3. Reactivation of cofiring patters is goal arm specific. Both, during the learning (top, orange) and the learned (bottom, green) condition, we computed the reactivation strength [Peyrache et al., 2010] of patterns observed during outward running for the sampling and the reward phase. For each session, reactivation was computed with respect to the true trial label (blue) and a swapped trial label (black). Left: For the true label reactivations were significantly (p_X) larger than for swapped labels expect for reward phase during learning. Right: Reactivation during sampling was significantly (p) larger than during reward for true trial labels (identity is illustrated by green solid line). P values were derived from Wilcoxon signed rank tests. Statistics are given in the main text.

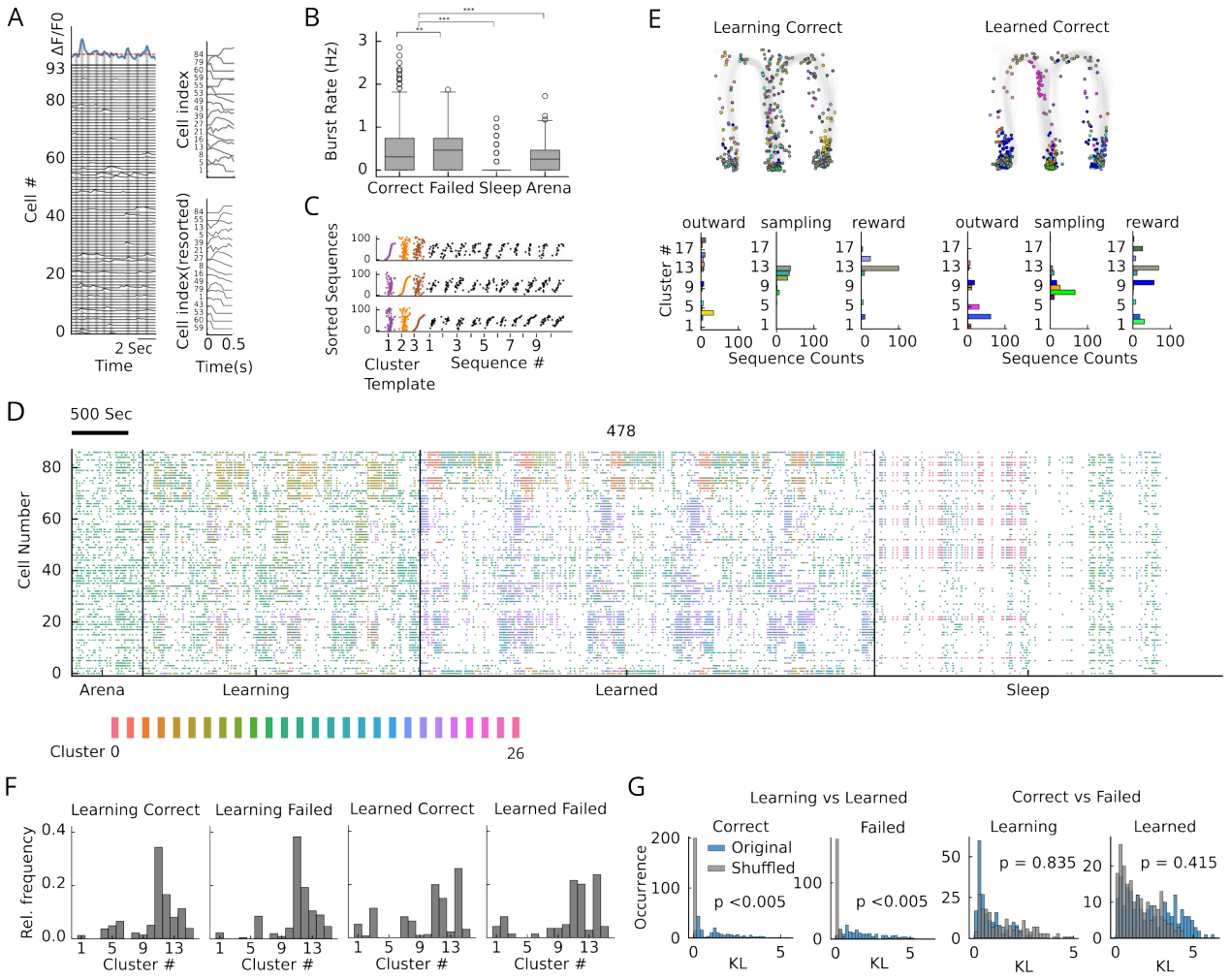

Figure 4. Recurring sequence motifs in 1-photon recordings change with learning. (A) Example population recording of 93 cells. Blue trace indicates population (sum) activity. Significant peaks (above red line) of population activity are identified as bursts. Within a 500 ms around burst peaks, cells are sorted according to the center of mass of the calcium trace. The index sorting is called a sequence. (B) Burst rates combined over all animals for different behavioral states. Correct and Failed correspond to Sampling, Outward and Reward from Fig. 1A, Sleep is derived from intermittent sleep epochs (see Methods), Arena denotes the habituation period where the animal was left in the arena without task (see Methods). Significance is derived from Mann-Whitney U rank tests (see main text). (C) Three example sequence cluster templates (colored) obtained via hierarchical clustering (see Methods) sorted according to first, second, and third cluster. Black sequences are representative cluster members of the cluster for which the cell index sorting was made in the panel. (D) Rastermap visualization [Supplement 2 to Figure 4 A; and Stringer et al., 2019] of sequences clusters (colors) for an example dataset from a single animal (478) for all sessions concatenated and sorted according to behavioral condition (Arena habituation, in task during Learning condition, in task during Learned condition, Sleep). Within each condition. Activity is ordered according to sessions and within each session intervals are ordered according to behavioral state (sampling, outward, reward, inward, Right, left respectively; see Supplement 2A to Figure 4 for illustration of ordering). Each point represents the time a cell had a calcium transient,

with colors indicating the active sequence cluster. Sleep sessions were dispersed throughout but shown here as a concatenated block for visualization purposes. (E, Top) Cluster identity (color) of a populations burst as a function of position on the maze in the learning and learned condition. (E, Bottom) Distributions of cluster identities for all burst in the behavioral phases. (F) Relative frequencies of cluster identities of bursts in one example animal during learning and in the learned condition subdivided for correct and failed trials. (G) Kullback-Leibler (KL) divergence of cluster distributions (as in panel F) for all animals (blue) were obtained by subsampling the number of bursts in the learned conditions to match the number of bursts in the learning conditions (see Methods). Animal-wise shuffles of learning and learned labels in the subsampled histograms are plotted in gray.

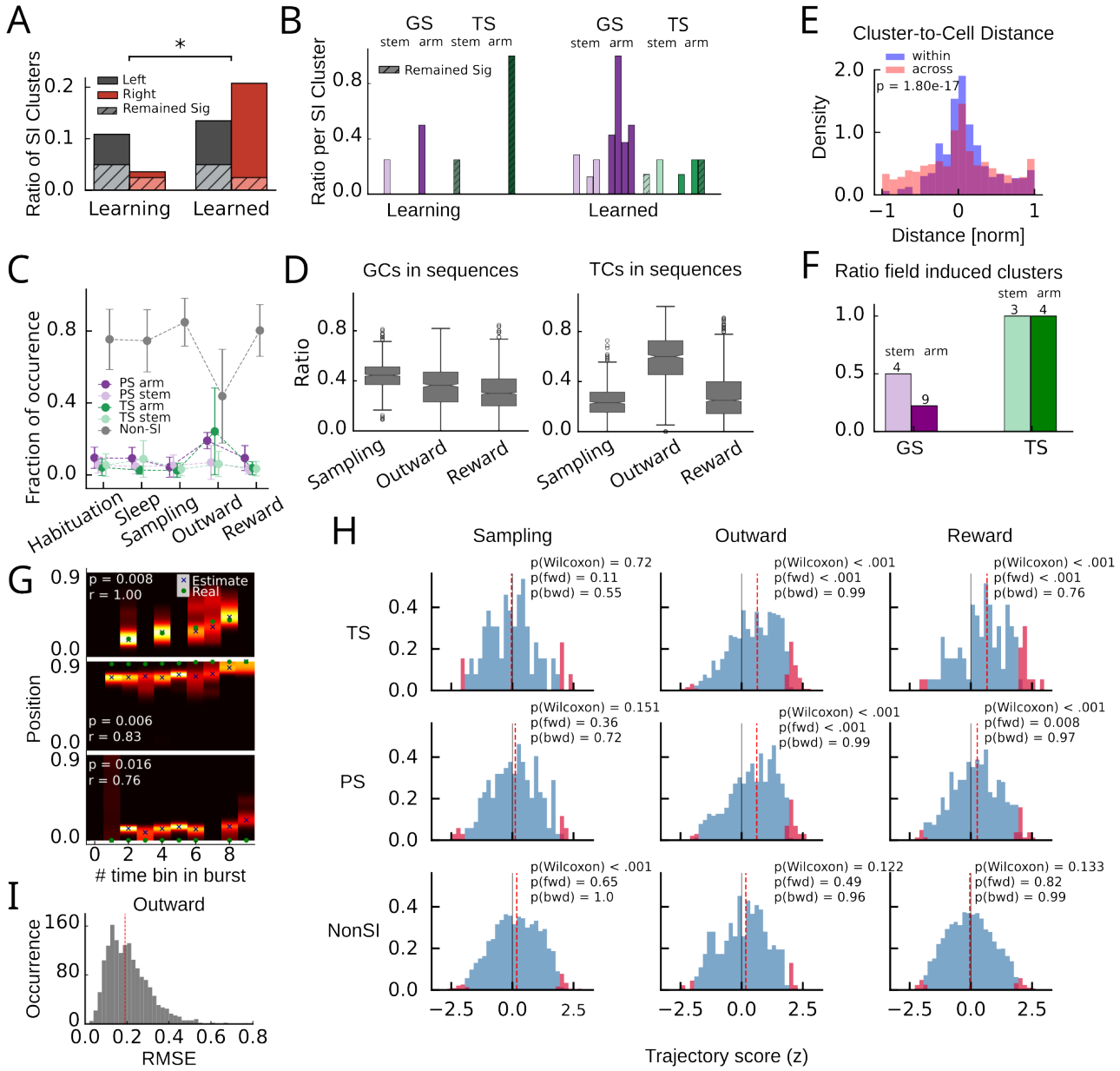

Figure 5. Generalized task phase- and goal arm selective sequences are used for replay but not planning. (A) Fraction of SI sequence clusters (relative to all clusters) combined across animals in the learning and learned condition. Hatched areas indicate proportions significant in both conditions. Significance is tested according to a Wilcoxon signed rank test (p=0.02). (B) Amount of GS and TS clusters normalized by the number of SI clusters for all 4 animals (individual bars) during learning and learned condition. Hatched areas indicate proportions of clusters remaining in the same category after learning. (C) Fraction of bursts attributed to GS, TS and non-SI sequence clusters during different behavioral phases. The majority of bursts is not selective to behavioral parameters except in the outward phase, where about half of the bursts are associated with behavior. (D) Fractions of GCs and TCs contributing to bursts of the different cluster types and different behavioral phases. (E) Histogram of distances between field peaks of the cluster and the field peaks

of the contributing cells for all SI clusters (blue). Distances between field peaks of all SI cells and all sequence clusters (across cluster) are shown in red. Clusters are called significantly cell induced if their absolute across cluster distances are significantly larger than the within cluster differences according to a one-sided Mann-Whitney U rank test. (F) Fraction of cell induced clusters (see panel E) during the learned condition. Number on top of bars indicate total numbers of clusters of that type over all animals. (G) Examples of decoding during bursts. Posterior is color coded (max normalized). Crosses indicate maximum posterior, green dots the true position of the animal in the respective time bin (50 ms). Top: Example during outward phase; Middle: example during reward phase; Bottom: example from odor sampling phase. (H) Distribution of z-scored rank order correlation coefficients between time bin and decoded position (trajectory scores) in each burst during sampling (left column), outward (middle column) and reward (right column) phase for generalized task phase-selective (top row), goal arm-selective (middle row) and non-SI (bottom row) clusters. Z-Scoring was performed using mean and standard deviation of a distribution obtained from randomly shuffling cell indices. Red bars indicate significant forward and backward replay for which trajectory score exceeded the upper 97.5 or the lower 2.5 percentile of the distribution generated by cell id randomization in the respective session. The fractions of forward and backward replay were then tested for significance above chance (0.025) according to a binomial test; p(fwd) & p(bwd). Red dashed lines indicate the medians, p(Wilcoxon) values are derived from a Wilcoxon signed rank test for zero median. (I) Distribution of RMSE from the outward phase over all animals (Red line indicates median).

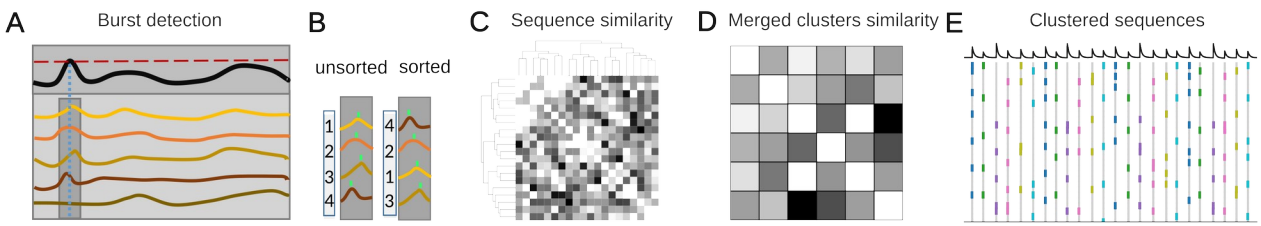

Figure 6. Schematized workflow of sequence detection. (A) For five example cells (calcium traces in colored lines) are summed to yield the population activity (black line). Whenever the population trace exceeds a threshold (red dashed line), a 500 ms second around the peak is considered a population burst (dark grey rectangle). (B) Single-cell activity within the 500 ms window is used to calculate center of mass for every cell. For every burst cells are reordered according to their center of mass. The resulting ordered indices are referred to as “sequence”. (C) A sequence similarity matrix is computed from the z-scored Spearman correlation between two sequences according to (Chenani et al., 2019); The binarized matrix (1: significant z value, 0: non significant z-value) is subject to hierarchical clustering. (D) Similarity z-scores are again computed for the all pairs of cluster templates (mean sequences in a cluster) and the clustering is iteratively repeated until merging criteria are no longer fulfilled. (E) Sorted sequences, with colors indicating cluster membership

Figure Supplements

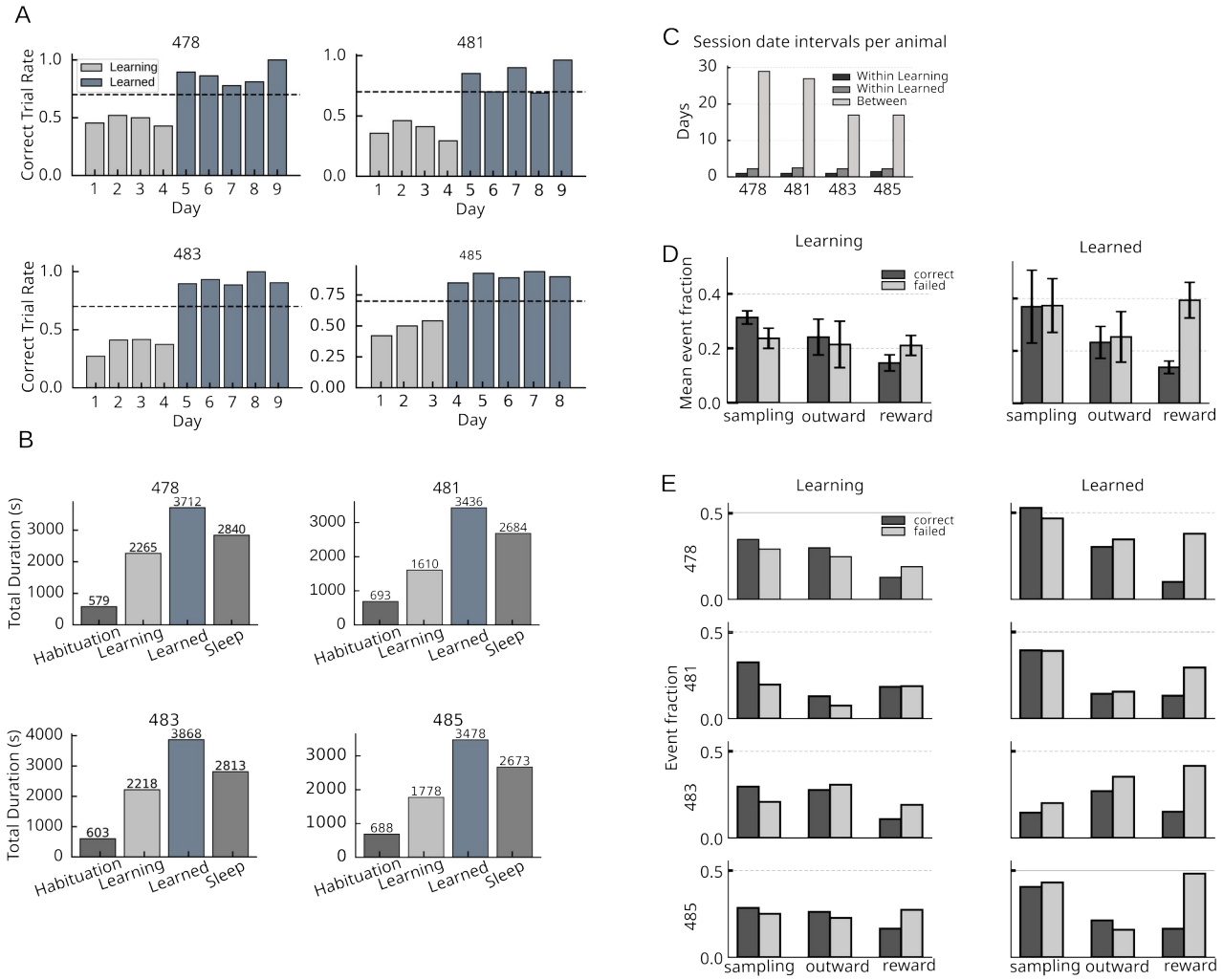

Supplementary Figure 1. (A) Ratios of correct trials the animals included in the study (487, 418, 483, 485). The dashed horizontal line at 0.70 indicates the criterion used to distinguish between learning and learned sessions. (B) Total duration of recordings spent in behavioral epochs for individual animals during habituation (arena), task learning, task learned, and sleep. (C) Intersession intervals for each animal. (D) Fractions of time covered by population bursts with sequences from identified clusters. (E) Same as D separated for each animal.

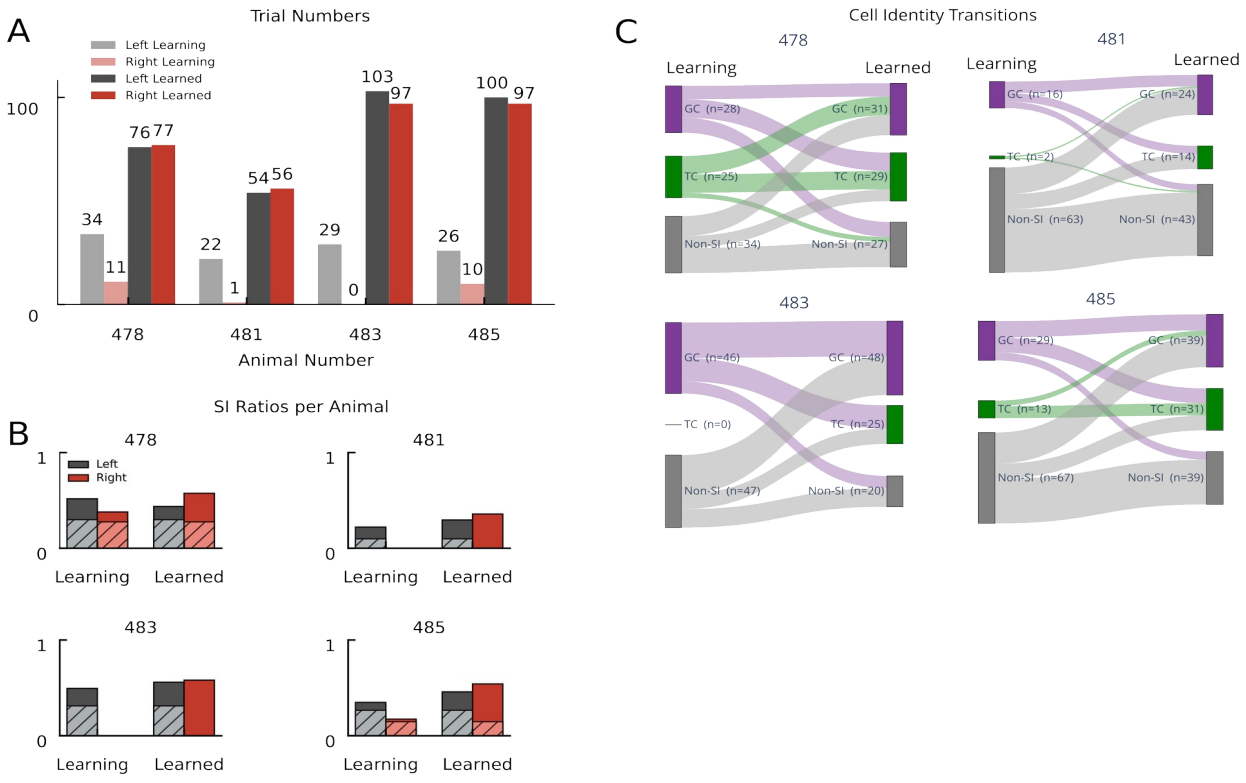

Supplement 1 to Figure 2. (A) Cumulative correct trial numbers of individual animals (478, 481, 483, 485) for left and right runs during learning and after learning (learned). (B) Fraction of SI cells in the learning and learned condition. Same as figure 2B, but shown separately for individual animals. Only correct trials are shown and used in the analysis. (C) Transitions of cell identity between learning and learned condition, presented for individual animals.

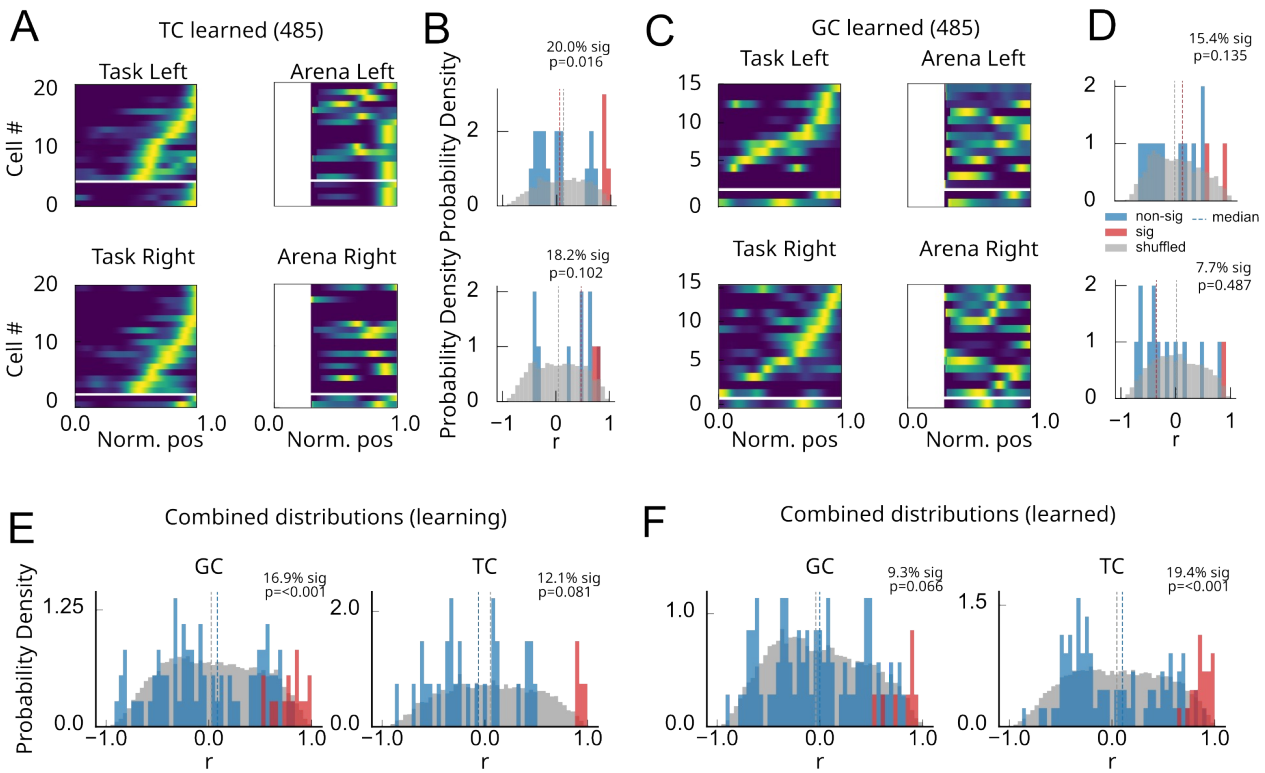

Supplement 2 to Figure 2. (A) Rate maps of TCs from an example animal (485) during proficient task performance (left) and arena habituation (without task; right). Because of the exploration pattern of the animals during arena habituation we could only compare the data mostly from the side arms. Stem areas with too little occupancy were excluded. Lower rows (separated by white stripe) depict cells with rate maps significantly similar between leaned condition an habituation. (B) Distribution of Pearson's correlation between place maps (blue/red). Red bars indicate significance with respect to circular shuffling of rate maps. Grey depicts shuffle distribution. P-values report significance of fractions of cells with significantly correlated rate maps (binomial test, 0.05). (C,D) Same as A,B for GCs. (E,F) Results cumulated over animals for the learning (E) and the learned (F) condition.

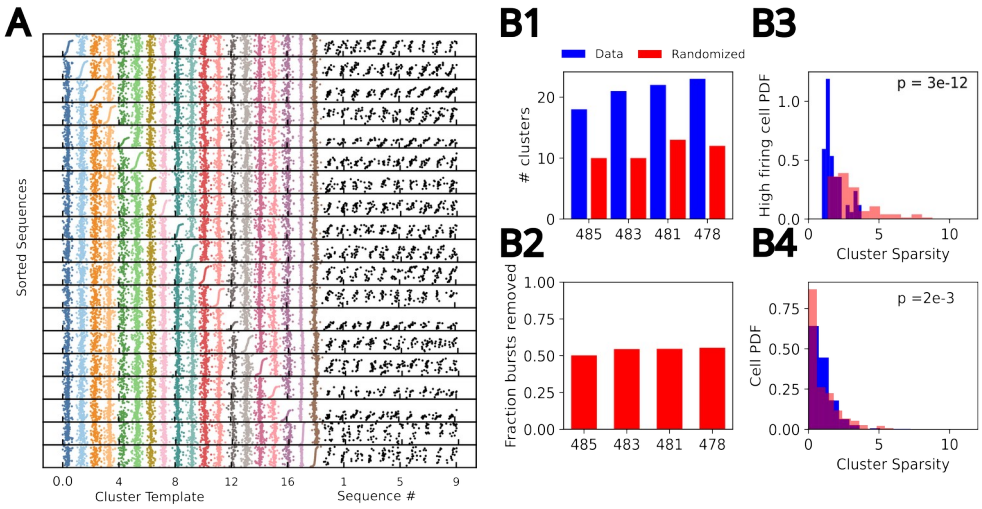

Supplement 1 to Figure 4. (A) Complete set of sequence cluster templates (colored) obtained via hierarchical clustering sorted according to cluster (see Fig. 4 C). Black sequences are representative cluster members of the cluster for which the cell index sorting was made in the panel. (B) Detected sequence clusters were obtained for the activation order derived from center of mass of the calcium trace (blue) and a randomized data set, where activation order was randomly permuted (red) for every burst (while keeping cell identities). (B1) Randomized data exhibit a much smaller number of sequence clusters in each animal. (B2) more than half of the bursts were no longer assigned a valid cluster in each animal (54% of all burst were removed on average over animals). (B3) Probability density function (pdf) of cluster sparsity for highly active cells (cells active in more than 20% of bursts). Sparsity was computed as 2nd divided by squared first moment of the distribution [Rolls and Tovee; 1995] normalized to the mean sparsity of the distribution for all (i.e., not just high firing) cells (B4). Normalization was performed to be able to compare across animals and across conditions (randomized/non-randomized) with largely different cluster counts. Cluster sparsity can be intuitively interpreted as how many more clusters a high firing cell is active in as compared to the mean number of clusters cells are active in on average. In randomized data, spurious clusters are dominated by few high-firing cells. Sparsity of high firing cells is significantly higher in randomized data (B3), whereas sparsity of high-firing cells is significantly lower over all cells (B4) reflecting the removal of a large number of bursts (B2). P-values are obtained via ranksum tests on the sparsity values.

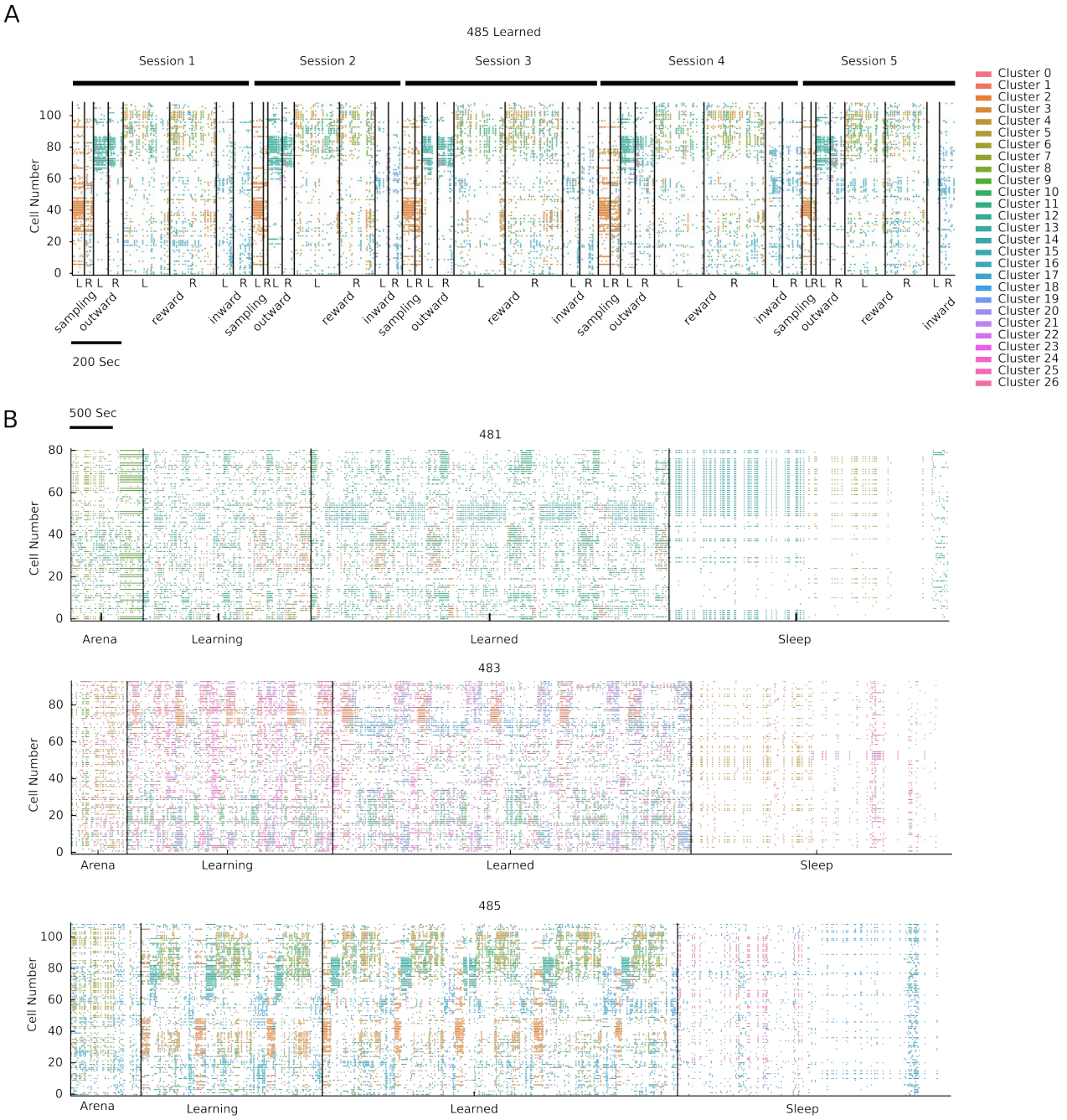

Supplement 2 to Figure 4. (A) Rastermap visualization [Stringer et al., 2019] (embedding dimension = 1, n_X=60) of clustered sequences for an example dataset from a single animal for all sessions in the learned condition concatenated. Each point represents the time a cell had a transient within a sequence, with colors indicating the sequence cluster. (B) Rastermap visualization of data from three more individual animals (482, 483, 485), including habituation and sleep sessions as in Fig. 4 D. Sleep sessions were dispersed throughout but shown here as a concatenated block for visualization purposes.

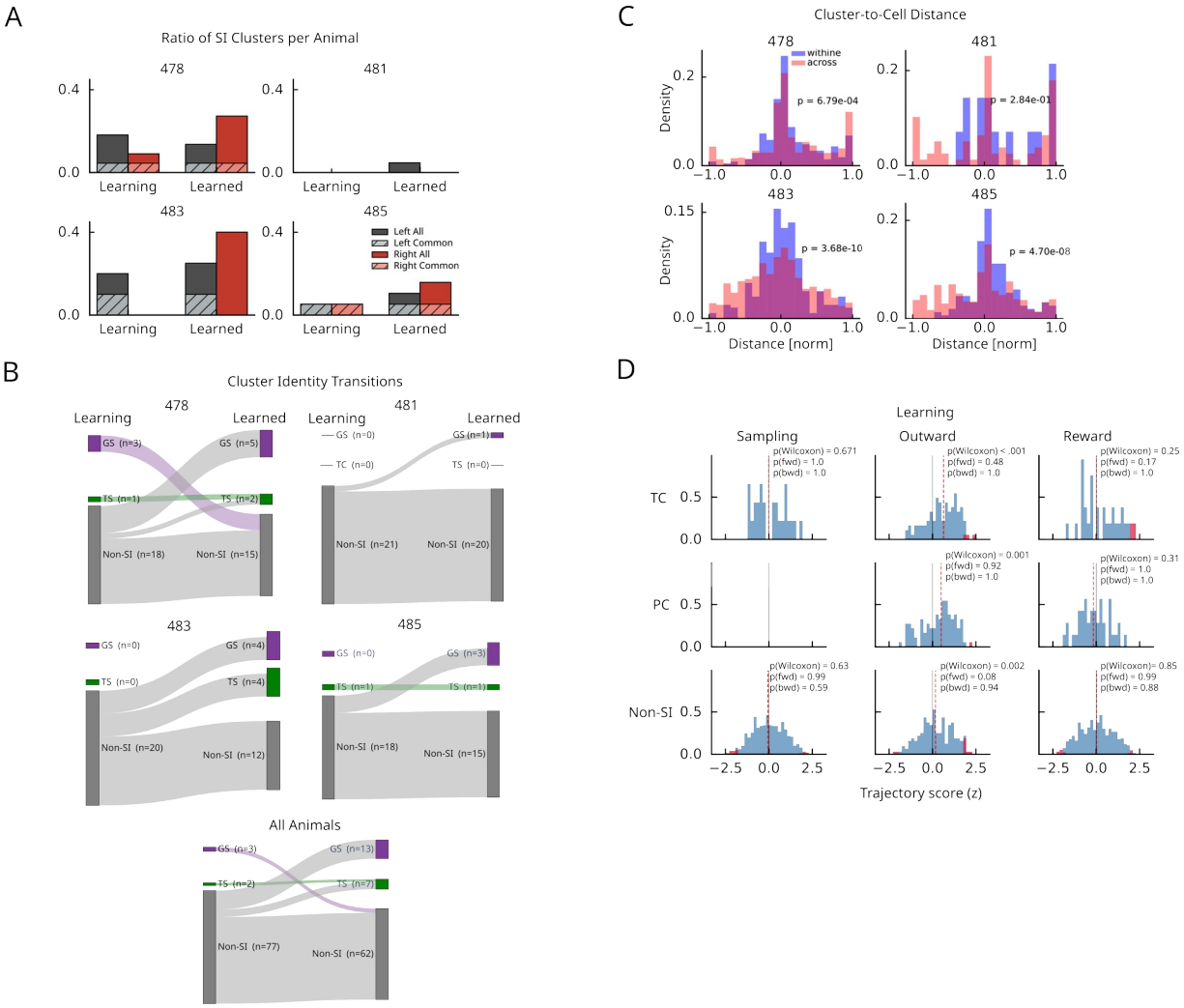

Supplement 1 to Figure 5. (A) Fraction of SI sequence clusters (relative to all clusters) for individual animals (478, 482, 483, 485) in the learning and learned condition. Hatched areas indicate proportions significant in both conditions. (B) Transitions of cluster identity between learning and learned condition, presented for individual animals and for the merged data of all animals. (C) Histogram of distances between field peaks of the cluster and the field peaks of the contributing cells. Same as Figure 4E, but shown separately for individual animals. (D) Distribution of behavioral correlations during learning. Same as Fig. 4H for the sessions in the learning condition. Only outward phase shows median significantly above zero.

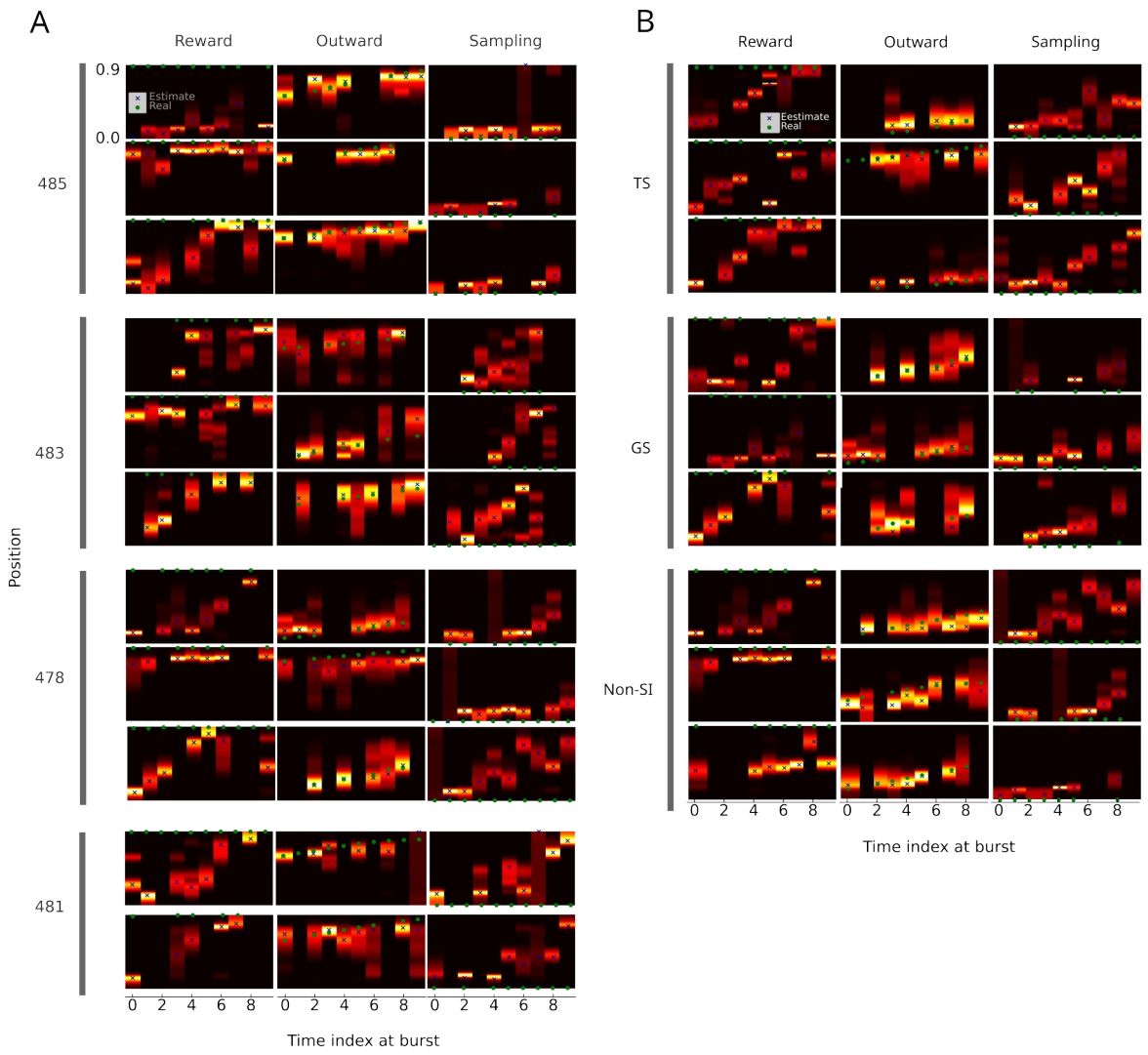

Supplement 2 to Figure 5. (A,B) Additional examples of decoding during bursts from different behavioral phases and cluster types (Same as Fig. 5G), ordered according to animal (A) or sequence type (B).